Long Distance Distributed Strain Sensing in OFDR by BM3D-SAPCA Image Denoising

Ming Pan, Peidong Hua, Zhenyang Ding [ID], Dongfang Zhu, Kun Liu [ID], Junfeng Jiang [ID], Chenhuan Wang [ID], Haohan Guo, Teng Zhang, Sheng Li, and Tiegen Liu [ID]

Abstract—We present a long distance distributed strain sensing in optical frequency domain reflectometry (OFDR) by shape-adaptive principal component analysis Block-Matching three-dimensional filter (BM3D-SAPCA) image denoising, which uses correlated patterns and high degree redundancy of sensing data for enhancing the performance of distributed sensing by image processing for removing noise and increasing the signal-to-noise ratio (SNR) of noisy measurements. Compared with 2D image denoising methods, BM3D-SAPCA method searches similar 2D image blocks and stacks them together in 3D arrays, which takes full advantage of the high level of similitude and redundancy contained on the multidimensional information to denoise. We find that the BM3D-SAPCA method can effectively suppresses noise aggravation along with an increasing of the sensing distance. Without modifying the hardware system of OFDR, we achieve a distributed strain sensing with a 5 cm spatial resolution, a 2 $\mu\varepsilon$ strain resolution on a 200 m all grating fiber. We compare the performance of distributed strain sensing by BM3D-SAPCA with Gaussian filter, wavelet denoising (WD) and non-local mean filter (NLM) using the same data. The mean maximal strain measurement error at loaded strain areas is reduced from 2.3791 $\mu\varepsilon$ to 0.6545 $\mu\varepsilon$ by BM3D-SAPCA. These mean errors by Gaussian filter, NLM and WD are 1.1177 $\mu\varepsilon$, 1.6668 $\mu\varepsilon$ and 1.9721 $\mu\varepsilon$, respectively. The mean standard deviations of strain measurement in eight repeat experiments is reduced from 1.5221 $\mu\varepsilon$ to 0.3134 $\mu\varepsilon$ after noise reduction by BM3D-SAPCA, which is 79.37% lower than the raw data. The mean standard deviations after noise reduction by Gaussian filter, NLM and WD are decreased by 68.85%, 64.24% and 14.41% respectively.

I. INTRODUCTION

DISTRIBUTED optical fiber sensing is indispensable to structural health monitoring, shape sensing, industry monitoring and so on [1], [2], [3]. Denoising is a key technology for performance of distributed optical fiber sensing. Soto et al. firstly exploited image denoising to remove noise in optical fiber sensors, which can provide a 100-fold improvement in the sensor performance with no hardware modification in a Brillouin optical time domain analysis (BOTDA) [4]. Image denoising are effective in Raman distributed temperature sensing [5] and phase sensitive optical time-domain reflectometer (φ-OTDR) system [6].

Optical frequency domain reflectometry (OFDR) can achieve a distributed strain sensing with high spatial resolution and high sensitivity. Froggatt et al. proposed a distributed strain and temperature sensing based on of Rayleigh backscattering spectra (RBS) shift in OFDR [7], [8]. Image denoising is also effective in OFDR based distributed sensing. The cross-correlation results of each fiber segment in the fiber under test (FUT) will be arranged along the fiber position to obtain a 2D image. Because of the high level of similitude and redundancy of information contained in the 2D image, image denoising can be efficient in removing random noise. After applying image denoising means on the 2D image, the quality of the cross-correlation results for each fiber segment will be improved. Zhao et al. used mean value filter, non-local mean filter (NLM), and wavelet denoising (WD) to realize a distributed strain sensing in OFDR with a sensing distance less than 12.5 m, spatial resolution of 0.4 mm and the strain measurement range of 50 $\mu\varepsilon$ to 500 $\mu\varepsilon$ [9]. Qu et al. used a total variation method and Gaussian filter to realize distributed strain sensing in OFDR with a sensing distance of 52 m, spatial resolution of 1.4 mm and the strain measurement range of 100 $\mu\varepsilon$ to 500 $\mu\varepsilon$ [10]. Qu et al. also used WD and Gaussian filter to realize a distributed strain sensing in OFDR with a sensing distance of less than 12 m, a spatial resolution of 4 mm and a strain measurement range of 3000 $\mu\varepsilon$ to 7000 $\mu\varepsilon$ [11]. Li et al. combined distance compensation and WD to achieve a distributed strain sensing in OFDR with a sensing distance of 25 m, a spatial resolution of 2.56 mm and a strain measurement range of 200 $\mu\varepsilon$ to 2000 $\mu\varepsilon$ [12].

TABLE I
RESEARCHES ON DISTRIBUTED STRAIN SENSING USING IMAGE PROCESSING IN OFDR

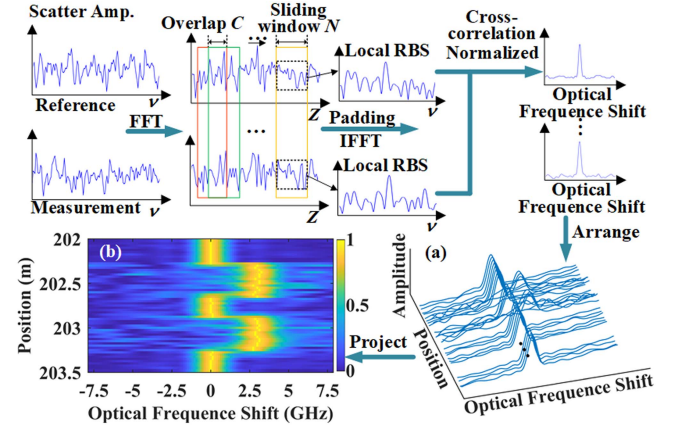| Work	Method	Sensing distance	Strain range	Spatial and Strain resolution
Ref. [9]	NLM, WD, Mean value filter	<12.5m	50 $\mu\varepsilon$- 500 $\mu\varepsilon$	0.4 mm; 50 $\mu\varepsilon$
Ref. [10]	Total variation, Gaussian filter	52 m	100 $\mu\varepsilon$- 500 $\mu\varepsilon$	1.4 mm; 100 $\mu\varepsilon$
Ref. [11]	WD, Gaussian filter	<12 m	3000 $\mu\varepsilon$- 7000 $\mu\varepsilon$	4 mm; 1000 $\mu\varepsilon$
Ref. [12]	DC+WD	25 m	200 $\mu\varepsilon$- 2000 $\mu\varepsilon$	2.56 mm; 200 $\mu\varepsilon$
Proposed method	BM3D-SAPCA	200 m	2 $\mu\varepsilon$- 24 $\mu\varepsilon$	5 cm; 2 $\mu\varepsilon$

Fig. 1. Preprocess for 2D image in OFDR. (a) Cross-correlation distribution by arranging all cross-correlation results along the corresponding positions of the FUT. (b) 2D cross-correlation image that is from projecting the cross-correlation distribution into 2D plane.

Table I lists the sensing performance of distributed strain sensing in OFDR based on different image processing methods. These researches above have realized distributed strain sensing of high spatial resolution and large strain measurement range in OFDR. However, the sensing distance and strain resolution are not good enough for some applications. A longer distance and smaller strain resolution in OFDR by image denoising has not been investigated so far.

These image denoising methods mentioned above such as NLM, WD, Gaussian filter belong to 2D data denoising, which are only performed in the spatial domain or wavelet domain and the denoising effect is limited. Dabov et al. firstly proposed a Block-Matching three-dimensional filter (BM3D), which exploits a specific nonlocal image modeling through a procedure termed grouping and collaborative filtering to realize a 3D data denoising. Grouping finds mutually similar 2D image blocks and stacks them together in 3D arrays. Collaborative filtering produces individual estimates of all grouped blocks by filtering them jointly, through transform-domain shrinkage of the 3D arrays [13]. BM3D has been widely used in imaging denoising in the field of radar [14], ultrasound [15] and optical coherence tomography [16]. In distributed optical fiber sensing, Wu et al. used BM3D to reduce the effect of random noise in Brillouin optical time-domain analyzer (BOTDA) [17]. Katkovnik and Foi et al. proposed local polynomial approximation-intersection of confidence intervals (LPA-ICI) method for image deblurring and edge detection [18], [19]. Muresan et al. applied adaptive principal component analysis (PCA) method on image denoising, which performs well in terms of image visual fidelity [20]. Dabov et al. also presented a shape-adaptive principal component analysis BM3D (BM3D-SAPCA), which extracted adaptive shape neighborhood of image blocks through 8-diectional LPA-ICI method and applied PCA transform on each adaptive shape neighborhoods part of 2D transform in 3D transform [21].

We present a long distance distributed strain sensing in OFDR by BM3D-SAPCA image denoising. Compared with 2D image denoising method, BM3D method searches similar 2D image blocks and stacks them together in 3D arrays, which takes full advantage of the high level of similitude and redundancy contained on the multidimensional information to denoise. We find that the BM3D-SAPCA method can effectively suppresses noise aggravation along with an increasing of sensing distance. Without modifying the hardware system of OFDR, we achieve a distributed strain sensing with a 5 cm spatial resolution, a 2 $\mu\varepsilon$ strain resolution on a 200 m all grating fiber. The sensing performance of distributed strain sensing in OFDR by BM3D-SAPCA is also shown in Table I. The sensing distance and strain resolution are enhanced greatly compared with other image denoising methods in OFDR [9], [10], [11], [12]. We compare the performance of distributed strain sensing by BM3D-SAPCA with Gaussian filter, WD and NLM using the same data. The mean maximal strain measurement error at loaded strain areas is reduced from 2.3791 $\mu\varepsilon$ to 0.6545 $\mu\varepsilon$ by BM3D-SAPCA. These mean errors by Gaussian filter, NLM and WD are 1.1177 $\mu\varepsilon$, 1.6668 $\mu\varepsilon$ and 1.9721 $\mu\varepsilon$, respectively. The mean standard deviations of strain measurement in eight repeat experiments is reduced from 1.5221 $\mu\varepsilon$ to 0.3141 $\mu\varepsilon$ after noise reduction by BM3D-SAPCA, which is 79.37% lower than the raw data. The mean standard deviations after noise reduction by Gaussian filter, NLM and WD are decreased by 68.85%, 64.24% and 14.41% respectively.

II. PRINCIPLE

A. Preprocessing

Fig. 1 shows the process of converting 1D distributed sensing information into 2D image in OFDR [9]. First, OFDR system collects data twice, one is the reference signal with no strain applied on the FUT, and the other is the measurement signal with strain. The signals are converted from optical frequency ν domain to distance z domain after fast Fourier transform (FFT) to get the Rayleigh scattering along the FUT. In the distance domain, a sliding window of size N with an overlap of size C is used to separate entire FUT to several fiber segment [9]. The adjacent information in the spatial domain is unitized in image denoising, so more spatial domain data points contribute
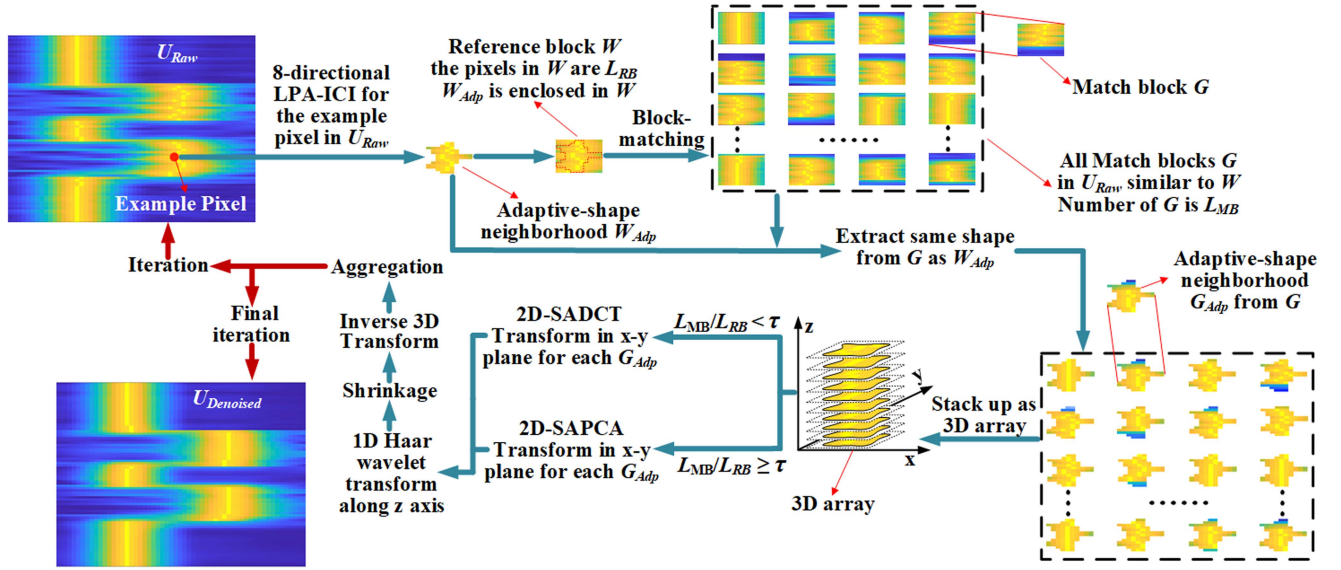
Fig. 2. Process of BM3D-SAPCA denoising 2D image in OFDR. U_{Raw} is the raw 2D cross-correlation image obtained by the cross-correlation arranged in the order of FUT positions. W_{Adp} is adaptive-shape neighborhood centered at the example pixel using 8-LPA-ICI. W is the reference block enclosing W_{Adp}. G is the match block similar to W in U_{Raw}. G_{Adp} is the adaptive-shape neighborhood by extracting the same shape as W_{Adp} from G. G_{Adp} lies on the x-y plane of 3D array, stacked along the z axis. $U_{Denoised}$ is the denoised result after the third iteration.

to image denoising. The overlap strategy can increase spatial domain data points and decrease the deterioration effect on the sensing spatial resolution when using image denoising, which has been explained in [9] in detail. The overlap between adjacent spatial segments caused a slight impact on the sensing spatial resolution, which will be verified by the experiment in Section IIIB. Padding M zeros is applied on each fiber segment and the size of fiber segment is $M + N$ [22]. Then, each fiber segment is converted to local RBS after inverse Fourier transform (IFFT). A normalized cross-correlation is applied on each reference and measurement local RBS. Similar cross-correlation calculations are performed for all fiber segments along FUT. Fig. 1(a) is a cross-correlation distribution obtained by arranging all cross-correlation results along the corresponding positions of the FUT. Fig. 1(b) is a 2D cross-correlation image after projecting the cross-correlation distribution into 2D plane. The color of each pixel on the 2D cross-correlation image in Fig. 1(b) represents the amplitude of cross-correlation distribution.

B. Principle of BM3D-SAPCA Based Image Denoising in OFDR

In OFDR based distributed strain sensing, the sensing distance and strain resolution are related to SNR of the system. Longer sensing distance will cause a worse SNR. At the same time, a better measurable strain resolution and sensing resolution will require a higher SNR. Denoising is a key technology for enhancing the performance of distributed strain sensing in OFDR. In this section, we will introduce the denoising process of BM3D-SAPCA for 2D cross-correlation image in OFDR.

Fig. 2 is the denoising process of BM3D-SAPCA for 2D cross-correlation images in OFDR. Firstly, we apply block grouping processing. U_{Raw} is the raw 2D cross-correlation

image obtained by the cross-correlation distribution arranged at the order of FUT positions. In order to demonstrate the denoising process clearly, U_{Raw} only demonstrates the strain area on FUT. A pixel in U_{Raw} is used as an example to explain the BM3D-SAPCA denoising process. We obtain an adaptive-shape neighborhood image block W_{Adp} centered at the current pixel by using the 8-directional LPA-ICI [18], [19], [21]. By comparing varying-scale directional kernel estimates, 8-LPA-ICI adaptively selects a set of directional adaptive scales for the pixel. Therefore, the edge and details of the denoised image can be maintained. The neighborhood of W_{Adp} is enclosed within a fixed-size and non-adaptive square block and W_{Adp} is converted to the reference block W. The number of pixels in W is L_{MB}. We search blocks G in U_{Raw} that are similar to W using block matching based on Euclidean distance. The number of G is L_{MB}. Adaptive-shape neighborhood G_{Adp} is extracted from each G using the same shape as W_{Adp}. A 3D array as a block grouping is stacked by G_{Adp}.

Secondly, we perform collaborative filtering on the 3D array. The 3D transformation of the 3D array is realized by using the combined an x-y plan 2D transformation and a z axis 1D transformation. We assume that a threshold τ is used to determine the 2D transform for G_{Adp} in the 3D array. If $L_{MB}/L_{RB} < \tau$, a 2D shape adaptive discrete cosine transform (2D-SADCT) transform is applied on x-y plan for each G_{Adp} because no enough G_{Adp} are found during the block matching process for 2D shape adaptive principal component analysis (2D-SAPCA) transform. In 2D-SADCT, adaptive shape neighborhoods are used to obtain the spectrum of image blocks, which improves the sparse representation of images and realizes the protection of edges and singularities [23]. If $L_{MB}/L_{RB} \geq \tau$, we apply 2D-SAPCA transform on x-y plan for each G_{Adp}. In 2D-SADCT, the transform basis is fixed for any given shape, so the data
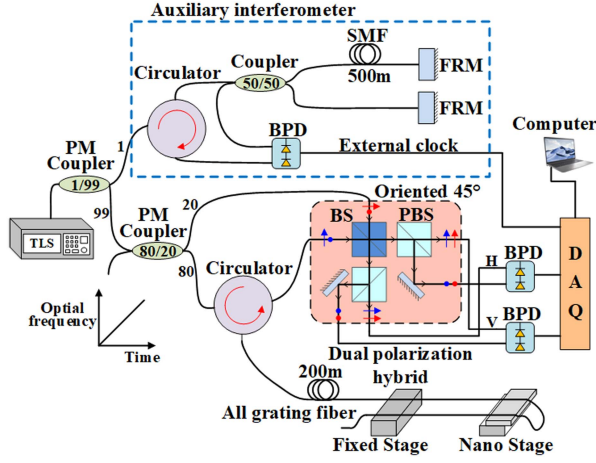
Fig. 3. OFDR system configuration diagram. TLS is tunable laser source. FRM is faraday rotating mirror. BPD is balanced photo-detector. DAQ is data acquisition card. BS is polarization insensitive beam splitter. PBS is polarization beam splitter. PM is polarization maintaining. The length of all grating fiber as FUT is about 200 m. The piezo-nanometer stage is used to apply the strain on the end of FUT. To set two adjacent strain applying areas, FUT pass through the nanometer stage twice. The distance between the fixed stage and nano stage is 40 cm, and the distance interval between the two strain applying areas is 20 cm.

adaptability is poor. 2D-SAPCA has good data adaptability, but requires enough image blocks to reliably implement the transformation [20], [24]. After 2D transform on the 3D array, a 1D Haar wavelet transform is applied on the z-axis of the 3D array. Then, we perform shrinkage on the 3D spectrum. The 3D array transformation effectively utilizes the shared features among all G_{Adp}, so noise can be effectively reduced when performing spectral coefficient shrinkage. The detailed explanation of 3D array transformation is explained in [13], [23], [24].

Thirdly, we reconstruct a denoised 2D cross-correlation image. We apply an inverse 3D transform on the 3D array to obtain estimates of each G_{Adp}. The inverse 3D transform are composed of inverse 1D Haar wavelet transform and inverse 2D transform in Fig. 2. After processing the above steps for each pixel in U_{Raw}, estimates of all G_{Adp} are aggregated based on their original locations using weighted averaging in case of overlapping. The aggregation result is a preliminary denoised image.

In order to ensure a better denoising effect, BM3D-SAPCA adopts three iterations. The shrinkage uses hard thresholding on wavelet coefficients. Then, an empirical Wiener filter is used to further improve the quality of filtering [25]. After these three iterations of denoising, the final noise reduction result is $U_{Denoised}$. The true optical frequency shift of each fiber segment on the $U_{Denoised}$ is recovered.

III. EXPERIMENTS AND DISCUSSIONS

A. OFDR System Configuration

We firstly describe the system configuration of OFDR shown in Fig. 3. The initial wavelength, tuning rate and tuning range ΔF of TLS (TLB-8800H, Newport Inc.) are 1553 nm, 3.75×10^4 GHz/s (300 nm/s), and 4.17×10^3 GHz (33.33 nm). The number of sampling points for the system to run once is 20 mega-samples (MS). The sensing spatial resolution is $\Delta X = N\Delta z$, where the

system spatial resolution $\Delta z = c/2n\Delta F$. c is the speed of light in vacuum. n is the refractive index of the fiber and has a magnitude of 1.46. The sliding window N is 2000. The overlap size C of the sliding window is 1000. The optical frequency resolution $\delta f = \Delta F/(M + N)$. The size of padding zero M is 30000. The sensing spatial resolution ΔX is 5 cm and optical frequency domain shift δf is 0.1302 GHz. A 1: 99 polarization maintaining (PM) coupler is used to split the light from the TLS into a main interferometer and an additional interferometer. 1% of the light is sent to the auxiliary Michelson interferometer. The auxiliary interferometer provides an external clock to trigger data acquisition (DAQ), which is used to collect the main interference signal at a uniform optical frequency. Since the length of FUT is about 200 m, the length of the delay fiber in the auxiliary interferometer is chosen to 500 m based on Nyquist theorem. 99% of the light is sent to the main Mach-Zehnder interferometer. Then, the light is further split by a 20:80 PM coupler, where 20% of the light is used as the reference light and 80% of the light is sent to the FUT through the circulator. The backscattered Rayleigh light is mixed with the reference light from the reference path in the 180 degrees dual polarization hybrid (Kylia Inc.) shown in the dotted-line box of Fig. 3, which contains two free-space polarization beam splitters (PBSs) and a free-space polarization insensitive beam splitter (BS). In the reference arm of the main Mach-Zehnder interferometer, the axis of the PM coupler inputting to dual polarization hybrid is oriented 45 degrees to the optical axis of two PBSs such that the reference light is equally split by two PBSs. The interference signals of the H and V channels are detected by the balanced photodetector (BPD). The combine of electronic signals of H and V channels are sent to the DAQ. The computer is used to process the data transferred from the DAQ by PCI Express.

In order to improve the SNR of OFDR signals, we use an all grating fiber (LBL-1550-125, FBGS Inc.) as the FUT. All grating fiber is an optical fiber containing densely spaced low reflective grating, which has a stronger backscattering than that of a standard single mode fiber [26]. The length of all grating fibers as FUT is about 200 m. Strain is precisely induced by a piezo-nanometer stretch stage at the end of FUT. One end of the tested portion of FUT is fixed on the fixed-stage and the other end is fixed on the piezo-nanometer stage. To set two adjacent strain areas, FUT passes through the nanometer stage twice. The distance between the fixed stage and nanometer stage is 40 cm, and the distance interval between these two strain areas loaded is 20 cm. Through the change of the nanometer stage, a static strain is applied to the part of FUT. The maximal measurable strain variation 25 $\mu\varepsilon$ is limited to the moving range of the piezo-nanometer stage about 10 μm.

B. Distributed Strain Sensing by Image Denoising Based on BM3D-SAPCA, Gaussian Filter, NLM and WD

To verify the denoising effect of BM3D-SAPCA on 2D-cross-correlation image, we loaded a static strain of 22 $\mu\varepsilon$ by the piezo-nanometer stage. Fig. 4 shows 2D cross-correlation image before and after Gaussian filter [27], NLM [28], WD [29] and BM3D-SAPCA at the strain area on FUT. Fig. 4(a) is the raw 2D
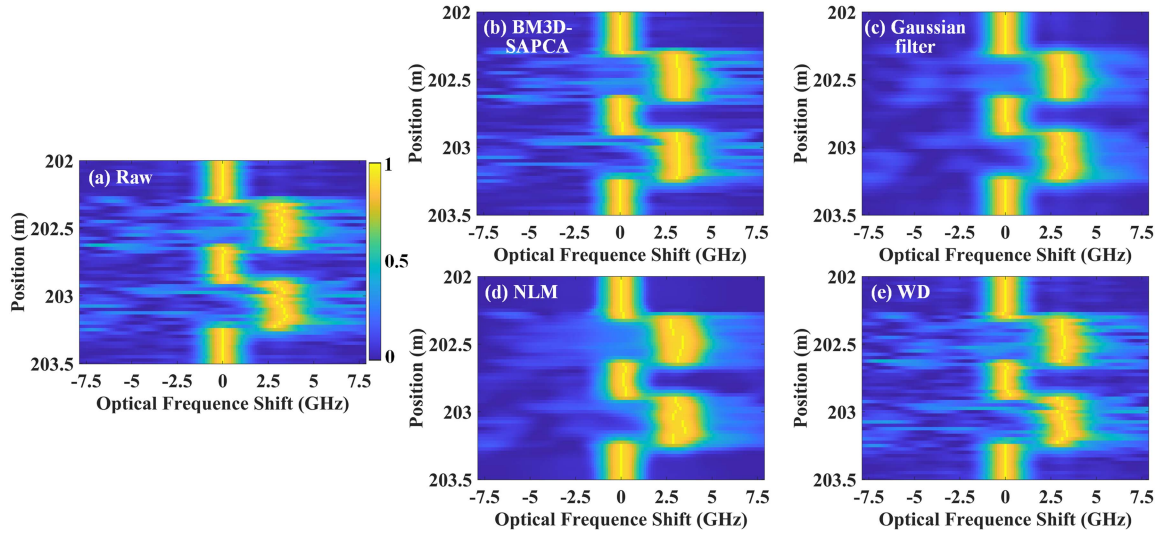
Fig. 4. 2D cross-correlation image before (a) and after BM3D-SAPCA (b), Gaussian filter (c), NLM (d) and WD (e). We apply 22 $\mu\varepsilon$ strain at the end of 200 m FUT. The stretch position length is 40 cm. The interval between the two stretching positions is 20 cm. The sensing spatial resolution is 5 cm. The overlap of adjacent fiber segment is 2.5 cm, which corresponds to half of the spatial resolution.

cross-correlation image, where these peaks in cross-correlation results at these two strain areas occurs optical frequency shift. In the ideal situation, the optical frequency shift occurring at the stain area should be consistent due to the uniform static strain applied on the FUT. However, the actual optical frequency shifts are affected by noise and become cluttered. Fig. 4(b) is the result of denoising the raw 2D cross-correlation image with BM3D-SAPCA. Compared with the raw 2D cross-correlation image, the optical frequency domain shifts of these peaks in cross-correlation results at these two strain areas become stable and mostly uniform, which means that BM3D-SAPCA can effectively reduce the interference of random noise and identify the strain with a size of 22 $\mu\varepsilon$. In order to demonstrate the superiority of the BM3D-SAPCA, we use Gaussian filter, NLM and WD to process the same data respectively, corresponding to Fig. 4(c)-(e). These three denoising methods can also suppress noise, but optical frequency shifts of these peaks in cross-correlation results at these two strain areas are still not stable and consistent. Therefore, among these denoising methods, BM3D-SAPCA has the best noise suppression effect on random noise and the worst is WD.

We apply different strain on FUT to compare the performance of distributed strain sensing by image denoising based on BM3D-SAPCA, Gaussian filter, NLM and WD shown in Fig. 5. At $\Delta X = 5$ cm, we load 12 sets strain under a strain range of 2 $\mu\varepsilon$ to 24 $\mu\varepsilon$ with a step size of 2 $\mu\varepsilon$. Fig. 5(a) shows the optical frequency shift distribution demodulated by raw data. We find that the optical frequency shifts at these two strain areas are inconsistent due to the influence of noise. The optical frequency shift curve at intervals of 2 $\mu\varepsilon$ are aliased and different loaded strain cannot be identified. Fig. 5(b) shows the optical frequency shift distribution demodulated by BM3D-SAPCA. It can be seen that the optical frequency shifts become mostly uniform at the strain area and different loaded strain with an interval of 2 $\mu\varepsilon$ can be clearly identified. The minimum measurable strain

of 2 $\mu\varepsilon$ can be successfully measured. Fig. 5(d)-(f) show the optical frequency shift distribution demodulated by Gaussian filter, NLM and WD, respectively. The optical frequency shifts are still not uniform at the strain area and different loaded strains with an interval of 2 $\mu\varepsilon$ are aliased. Compared with the denoising methods mentioned above, BM3D-SAPCA has the best denoising performance, the worst performing denoising method is WD.

The linear fitting curve between loaded strains and optical frequency shifts demodulated by BM3D-SAPCA denoising is shown in Fig. 5(c). We find that the optical frequency shift and the strain variation have a good linear relationship, which R-squared is 0.9972. The root mean squared error (RMSE) is 0.0651. The calibration coefficient is 0.151 GHz/$\mu\varepsilon$.

In order to quantitatively evaluate optical frequency shift distribution at the strain area demodulated by BM3D-SAPCA, Gaussian filter, NLM and WD denoising, we calculated the standard deviation of optical frequency shifts caused by 12 sets loaded strain at these two strain areas. The smaller standard deviation of optical frequency shifts reflects that the demodulated strain is the more uniform at the strain area. The mean of all standard deviations $Mstd$ can be expressed as:

$$Mstd = \sum_{i=1}^{12} Std_i / 12, \tag{1}$$

$$Comp = (Mstd - Mstd_{Raw}) / Mstd_{Raw} \times 100\%, \tag{2}$$

where Std_i is the standard deviation at the strain area for each setting strain. $Mstd_{Raw}$ is the mean standard deviation of raw data. $Comp$ is the change rate of mean standard deviation after denoising.

Table II shows the mean standard deviation of the optical frequency shift caused by 12 sets loaded strain at these two strain areas. It can be seen that the mean standard deviation at these
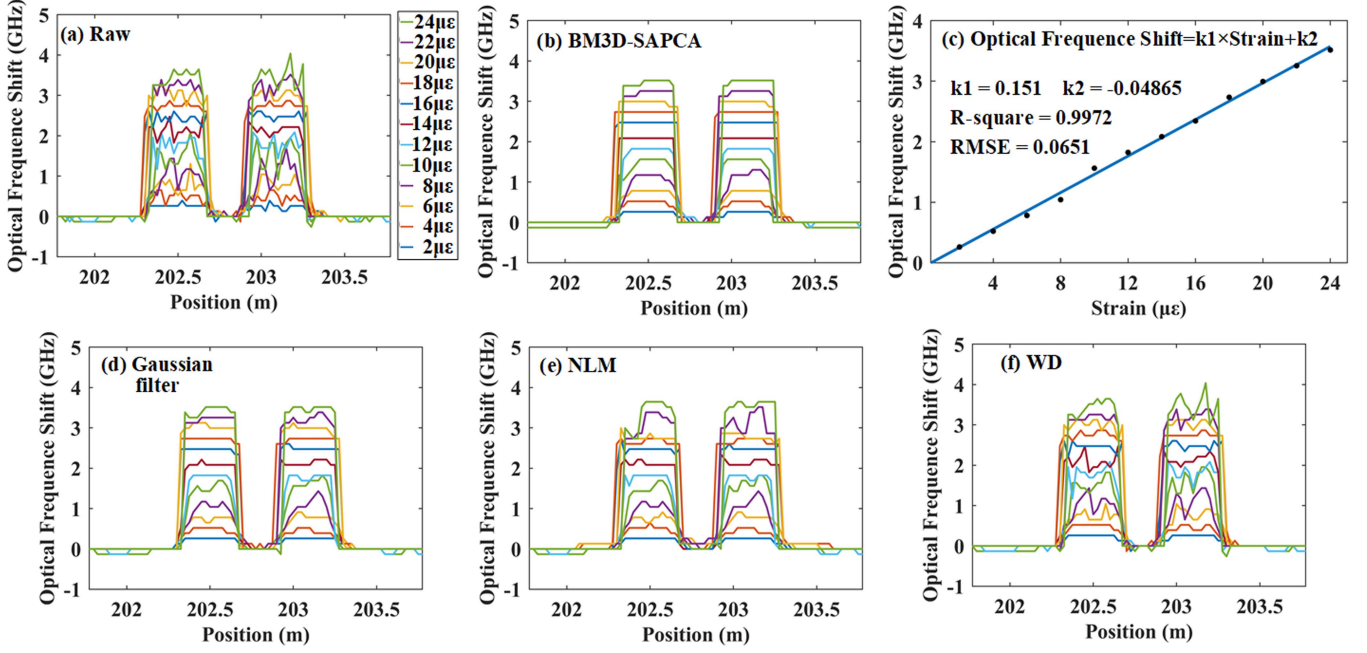
Fig. 5. Optical frequency shift distribution caused by different loaded strain before (a) and after BM3D-SAPCA (b), Gaussian filter (d), NLM (e) and WD (f). Two strain areas with a range of 2 $\mu\varepsilon$ to 24 $\mu\varepsilon$ and a step of 2 $\mu\varepsilon$ are applied at the end of 200 m FUT. The stretch position length is 40 cm. The interval between the two stretching positions is 20 cm. The sensing spatial resolution is 5 cm. The overlap of adjacent fiber segment is 2.5 cm, which corresponds to half of the spatial resolution. (c) Linear fitting curve between loaded strains and optical frequency shifts demodulated by BM3D-SAPCA denoising.

TABLE II
MEAN STANDARD DEVIATIONS OF OPTICAL FREQUENCY SHIFT BEFORE AND AFTER DENOISING AT STRAIN AREAS WITH LOADED STRAINS FROM 2 $\mu\varepsilon$ TO 24 $\mu\varepsilon$

Methods	$Mstd_{Raw}$ (GHz)	$Mstd$ (GHz)	$Comp$ (%)
BM3D-SAPCA	0.1648	0.0211	↓87.21
Gaussian filter	0.1648	0.0605	↓63.29
NLM	0.1648	0.0989	↓39.99
WD	0.1648	0.1259	↓23.61

two strain areas is reduced from 0.1648 to 0.0211 after noise reduction by BM3D-SAPCA, which is 87.21% lower than the raw data. The mean standard deviations after noise reduction by Gaussian filter, NLM and WD are decreased by 63.29%, 39.99% and 23.61% respectively. The strain distribution demodulated by BM3D-SAPCA is the most uniform at strain areas among these image denoising methods.

Strain measurement error is also an important indicator to evaluate the denoising effect. Compared with the average strain measurement error as an indicator to evaluate the denoising effect, the maximum strain error can reflect the worst level of strain error before and after denoising. The strain is calculated from the optical frequency shift multiplying by the calibration coefficient in Fig. 5(c). We compare the strain measurement error processed by Gaussian filter, NLM, WD and BM3D-SAPCA. The maximal strain measurement error is expressed as:

$$\delta = \max\{|\varepsilon_i - \varepsilon_s|\}, \qquad (3)$$

where ε_i is the measured strain at the strain area. ε_s represents the setting strain by the nanometer stage.

Table III is the results of the strain measurement error. It can be seen that the δ on each setting strains is significantly reduced after BM3D-SAPCA processing and the mean of δ on each setting strains is reduced from 2.3791 $\mu\varepsilon$ to 0.6545 $\mu\varepsilon$. The mean of δ on each setting strains processed by Gaussian filter, NLM and WD are 1.1177 $\mu\varepsilon$, 1.6668 $\mu\varepsilon$ and 1.9721 $\mu\varepsilon$ respectively. The results of strain measurement error reflect BM3D-SAPCA can effectively reduce the strain measurement error and has obvious advantages than these three denoising methods above.

In order to quantitatively evaluate the performance and actual stability of the proposed BM3D-SAPCA method and other image denoising methods over time, we apply eight repeat experiments with loaded strain from 2 $\mu\varepsilon$ to 24 $\mu\varepsilon$. In each experiment, we take 16 strain measurement data points at these two strain positions, corresponding to 40 cm stretch positions. Therefore, we acquire 128 strain measurement data points from each loaded strain in these repeat eight experiments. The standard deviation of multi-times measurement is in repeat experiments is used to evaluate the stability and performance of denoising methods [4], [30]. We calculate the standard deviation of 128 data points of each loaded strain processed by raw data, BM3D-SAPCA, Gaussian filter, NLM and WD over time shown in Table IV. We use We also calculate the mean standard deviation of strain $MSStd$ based on (4) and change rate of $MSStd$ after denoising $SComp$ based on (5):

$$MSStd = \sum_{i=1}^{12} SStd_i / 12, \qquad (4)$$

TABLE III
ERROR OF STRAIN MEASUREMENT BEFORE AND AFTER DENOISING WITH LOADED STRAINS FROM 2 $\mu\varepsilon$ TO 24 $\mu\varepsilon$

Measured Strains (με)	δ Raw (με)	δ BM3D-SAPCA (με)	δ Gaussian filter (με)	δ NLM (με)	δ WD (με)
2	0.9091	0.0468	0.0468	0.0468	0.0468
4	1.9532	1.0909	1.0909	1.0909	1.0909
6	2.9453	0.5040	1.3663	1.3663	1.3663
8	3.5322	0.9453	1.8076	1.8076	3.3663
10	4.1191	0.6699	2.3945	2.3945	3.2568
12	2.1924	0.3945	0.4678	0.4679	2.1925
14	2.7060	0.1191	0.9814	0.9815	2.7061
16	1.5683	0.7060	0.7060	0.7061	1.5683
18	1.2929	0.4306	0.4306	0.4317	1.2929
20	1.5694	0.7071	1.0176	1.5694	1.0175
22	2.7071	0.9825	0.9825	3.5694	2.7071
24	3.0537	1.2578	2.1202	5.5694	3.0537
Mean	2.3791	0.6545	1.1177	1.6668	1.9721

TABLE IV
STANDARD DEVIATIONS OF STRAINS BEFORE AND AFTER DENOISING WITH LOADED STRAINS FROM 2 $\mu\varepsilon$ TO 24 $\mu\varepsilon$ IN EIGHT REPEAT EXPERIMENTS

Measured Strains (με)	Raw (με)	BM3D-SAPCA (με)	Gaussian filter (με)	NLM (με)	WD (με)
2	0.3902	0.0000	0.1830	0.1677	0.2126
4	5.9654	0.2426	0.4462	0.4116	5.9271
6	1.0854	0.2537	0.4395	0.4332	0.6881
8	1.7805	0.6559	0.7041	0.6822	1.5147
10	1.9148	0.5274	0.7467	0.8382	1.7427
12	1.4457	0.4013	0.6079	0.6097	1.0102
14	0.9673	0.2615	0.4709	0.4427	0.8057
16	0.5514	0.3078	0.4275	0.3143	0.4478
18	0.5661	0.1074	0.1830	0.4252	0.4557
20	0.8952	0.3302	0.3915	0.7221	0.5457
22	1.1780	0.3318	0.5017	0.9012	0.8774
24	1.5257	0.3490	0.5874	0.5830	1.4065
MSStd	1.5221	0.3141	0.4741	0.5443	1.3029
SComp (%)	↓0	↓79.37	↓68.85	↓64.24	↓14.41

$$SComp = (MSStd - MSStd_{Raw})/MSStd_{Raw} \times 100\%, \quad (5)$$

where $SStd_i$ is the standard deviation of 128 strain measurement data points for each loaded strain in eight repeat experiments.

$MSStd_{Raw}$ is the mean standard deviation of 12 groups loaded strain from 2 $\mu\varepsilon$ to 24 $\mu\varepsilon$ in raw data. $MSStd$ at these two strain areas is reduced from 1.5221 $\mu\varepsilon$ to 0.3141 $\mu\varepsilon$ after BM3D-SAPCA, which is 79.37% lower than the raw data. The mean standard deviations after Gaussian filter, NLM and WD
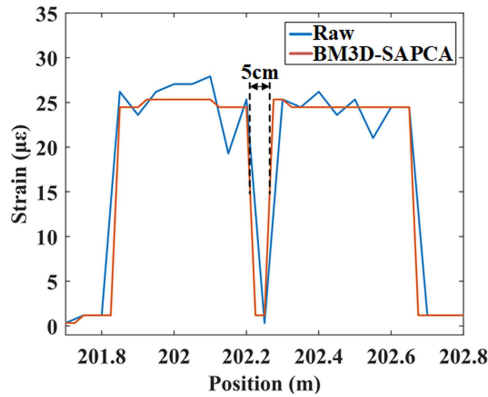
Fig. 6. Distributed strain sensing curve before and after BM3D-SAPCA. Two strain areas with 24 $\mu\varepsilon$ are applied at the end of 200 m FUT. The stretch position length is 40 cm. The interval between these two stretching positions is 5 cm, which illustrates the sensing spatial resolution can be up to 5 cm.

are decreased by 68.85%, 64.24% and 14.41% respectively. The standard deviations of each strain after BM3D-SAPCA are all smaller than those processed by Gaussian filter, NLM and WD. Therefore, the stability and performance of BM3D-SAPCA are the best among Gaussian filter, NLM and WD over time.

We apply an experiment to evaluate the sensing spatial resolution of this system. In this experiment, we set the interval between these two stretching positions to 5 cm, which is the claimed sensing spatial resolution. The stretch length is 40 cm, and apply a strain variation of 24 $\mu\varepsilon$ on these two stretching areas. The raw distributed strain sensing curve by a non-overlap siding window without image denoising is represented as a blue line in Fig. 6. The distributed strain sensing curve by an overlap siding window with BM3D-SAPCA is represented as a red line in Fig. 6. Compared with the raw data, these two strain with an interval of 5 cm processed by BM3D-SAPCA still can be distinguished, which illustrates the sensing spatial resolution can be up to 5 cm.

Although BM3D-SAPCA has great advantages in denoising performance, the processing efficiency is not well due to the complex computation of images in the spatial and wavelet domains. In the later stage, the graphics processing unit (GPU) can be used to realize parallel computing of the denoising process of BM3D-SAPCA, thereby improving the processing efficiency.

For noise model, Gaussian filter, NLM, WD is suitable for reducing white additive noise. BM3D-SAPCA is also suitable for reduce white additive noise [13], [24]. Based on white additive noise assumption, Gaussian filter, NLM, WD has a well denoising effects in OFDR [9], [10], [11], [12]. Therefore, BM3D-SAPCA similarly has a well denoising effects in OFDR. The noise in the OFDR cross-correlation spectrum is correlated noise. Whereas, the cross-correlation spectrum also contain additive noise component, so these image denoising methods are effective in OFDR. In the future, we will explore denoising methods for correlated noise in OFDR.

The well performance of this proposed OFDR based distributed sensing system is due to a combination of image denoising method and all grating fiber. All grating fiber is very

significant to SNR at a long sensing range of 200 m. To compare with different image denoising methods fairly, the same raw data of all grating fiber are processed by these image denoising methods. In this comparison, BM3D-SAPCA has the best performance among them.

IV. CONCLUSION

We present a long distance distributed strain sensing in OFDR by BM3D-SAPCA image denoising. Compared with 2D image denoising method, BM3D method searches similar 2D image blocks and stacks them together in 3D arrays, which takes full advantage of the high level of similitude and redundancy contained on the multidimensional information to denoise. We find that the BM3D-SAPCA method can effectively suppresses random noise aggravation along with an increasing of sensing distance. Without modifying the hardware system of OFDR, we achieve a distributed strain sensing with 5 cm spatial resolution, 2 $\mu\varepsilon$ strain resolution on a 200 m all grating fiber. We compare the performance of distributed strain sensing by BM3D-SAPCA with Gaussian filter, WD and NLM using the same data. The mean maximal strain measurement error at loaded strain areas is reduced from 2.3791 $\mu\varepsilon$ to 0.6545 $\mu\varepsilon$ by BM3D-SAPCA. These mean errors by Gaussian filter, NLM and WD are 1.1177 $\mu\varepsilon$, 1.6668 $\mu\varepsilon$ and 1.9721 $\mu\varepsilon$, respectively. The mean standard deviations of strain measurement in eight repeat experiments is reduced from 1.5221 $\mu\varepsilon$ to 0.3141 $\mu\varepsilon$ after noise reduction by BM3D-SAPCA, which is 79.37% lower than the raw data. The mean standard deviations after noise reduction by Gaussian filter, NLM and WD are decreased by 68.85%, 64.24% and 14.41% respectively.

REFERENCES

[1] J. M. Lopez-Higuera, L. R. Cobo, A. Q. Incera, and A. Cobo, "Fiber optic sensors in structural health monitoring," *J. Lightw. Technol.*, vol. 29, no. 4, pp. 587–608, Feb. 2011.

[2] Z. Ding et al., "Distributed optical fiber sensors based on optical frequency domain reflectometry: A review," *Sensors*, vol. 18, no. 4, 2018, Art. no. 1072.

[3] Y. Wang et al., "Millimeter-level-spatial-resolution Brillouin optical correlation-domain analysis based on broadband chaotic laser," *J. Lightw. Technol.*, vol. 37, no. 15, pp. 3706–3712, Aug. 2019.

[4] M. A. Soto, J. A. Ramirez, and L. Thevenaz, "Intensifying the response of distributed optical fibre sensors using 2D and 3D image restoration," *Nature Commun.*, vol. 7, 2016, Art. no. 10870.

[5] M. A. Soto, J. A. Ramirez, and L. Thevenaz, "Reaching millikelvin resolution in Raman distributed temperature sensing using image processing," *Proc. SPIE*, vol. 9916, 2016, Art. no. 99162A.

[6] H. He et al., "SNR enhancement in phase-sensitive OTDR with adaptive 2-D bilateral filtering algorithm," *IEEE Photon. J.*, vol. 9, no. 3, Jun. 2017, Art. no. 6802610.

[7] M. Froggatt and J. Moore, "High-spatial-resolution distributed strain measurement in optical fiber with Rayleigh scatter," *Appl. Opt.*, vol. 37, no. 10, pp. 1735–1740, 1998.

[8] S. T. Kreger, D. K. Gifford, M. E. Froggatt, B. J. Soller, and M. S. Wolfe, "High resolution distributed strain or temperature measurements in single- and multi-mode fiber using swept-wavelength interferometry," in *Proc. 18th Int. Conf. Opt. Fiber Sensors*, 2006, Paper ThE42.

[9] S. Zhao, J. Cui, Z. Wu, and J. Tan, "Accuracy improvement in OFDR-based distributed sensing system by image processing," *Opt. Lasers Eng.*, vol. 124, 2020, Art. no. 105824.

[10] S. Qu et al., "High spatial resolution investigation of OFDR based on image denoising methods," *IEEE Sensors J.*, vol. 21, no. 17, pp. 18871–18876, Sep. 2021.

[11] S. Qu, Z. Qin, Y. Xu, Z. Cong, Z. Wang, and Z. Liu, "Improvement of strain measurement range via image processing methods in OFDR system," *J. Lightw. Technol.*, vol. 39, no. 19, pp. 6340–6347, Oct. 2021.

[12] P. Li et al., "High-Spatial-Resolution strain sensor based on distance compensation and image wavelet denoising method in OFDR," *J. Lightw. Technol.*, vol. 39, no. 19, pp. 6334–6339, Oct. 2021.

[13] K. Dabov, A. Foi, V. Katkovnik, and K. Egiazarian, "Image denoising by sparse 3-D transform-domain collaborative filtering," *IEEE Trans. Image Process.*, vol. 16, no. 8, pp. 2080–2095, Aug. 2007.

[14] F. Argenti, A. Lapini, T. Bianchi, and L. Alparone, "A tutorial on speckle reduction in synthetic aperture radar images," *IEEE Geosci. Remote Sens. Mag.*, vol. 1, no. 3, pp. 6–35, Sep. 2013.

[15] C. A. N. Santos, D. L. N. Martins, and N. D. A. Mascarenhas, "Ultrasound image despeckling using stochastic distance-based BM3D," *IEEE Trans. Image Process.*, vol. 26, no. 6, pp. 2632–2643, Jun. 2017.

[16] L. Fang, S. Li, Q. Nie, J. A. Izatt, C. A. Toth, and S. Farsiu, "Sparsity based denoising of spectral domain optical coherence tomography images," *Biomed. Opt. Exp.*, vol. 3, no. 5, pp. 927–942, 2012.

[17] H. Wu, L. Wang, Z. Zhao, N. Guo, C. Shu, and C. Lu, "Brillouin optical time domain analyzer sensors assisted by advanced image denoising techniques," *Opt. Exp.*, vol. 26, no. 5, pp. 5126–5139, 2018.

[18] A. Foi, V. Katkovnik, K. Egiazarian, and J. Astola, "A novel anisotropic local polynomial estimator based on directional multiscale optimizations," in *Proc. 6th IMA Int. Conf. Math. Signal Process.*, 2004, pp. 79–82.

[19] V. Katkovnik, A. Foi, K. Egiazarian, and J. Astola, "Directional varying scale approximations for anisotropic signal processing," in *Proc. 12th Eur. Signal Process. Conf.*, 2004, pp. 101–104.

[20] D. D. Muresan and T. W. Parks, "Adaptive principal components and image denoising," in *Proc. Int. Conf. Image Process.*, 2003, pp. I–101.

[21] K. Dabov, A. Foi, V. Katkovnik, and K. Egiazarian, "A nonlocal and shape-adaptive transform-domain collaborative filtering," in *Proc. Int. Workshop Local Non-Local Approx. Image Process.*, 2008, pp. 1–8.

[22] J. Cui, S. Zhao, D. Yang, and Z. Ding, "Investigation of the interpolation method to improve the distributed strain measurement accuracy in optical frequency domain reflectometry systems," *Appl. Opt.*, vol. 57, no. 6, pp. 1424–1431, 2018.

[23] A. Foi, V. Katkovnik, and K. Egiazarian, "Pointwise shape-adaptive DCT for high-quality denoising and deblocking of grayscale and color images," *IEEE Trans. Image Process.*, vol. 16, no. 5, pp. 1395–1411, May 2007.

[24] K. Dabov, A. Foi, V. Katkovnik, and K. Egiazarian, "BM3D image denoising with shape-adaptive principal component analysis," in *Proc. Workshop Signal Process. Adaptive Sparse Structured Representation*, 2008, pp. 1–8.

[25] M. Kazubek, "Wavelet domain image denoising by thresholding and wiener filtering," *IEEE Signal Process. Lett.*, vol. 10, no. 11, pp. 324–326, Nov. 2003.

[26] C. Wang et al., "High sensitivity distributed static strain sensing based on differential relative phase in optical frequency domain reflectometry," *J. Lightw. Technol.*, vol. 38, no. 20, pp. 5825–5836, Oct. 2020.

[27] M. Mafi, H. Martin, M. Cabrerizo, J. Andrian, A. Barreto, and M. Adjouadi, "A comprehensive survey on impulse and Gaussian denoising filters for digital images," *Signal Process.*, vol. 157, pp. 236–260, 2019.

[28] A. Buades, B. Coll, and J. Morel, "A non-local algorithm for image denoising," in *Proc. IEEE Comput. Soc. Conf. Comput. Vis. Pattern Recognit.*, 2005, pp. 60–65.

[29] D. L. Donoho and I. M. Johnstone, "Ideal spatial adaptation by wavelet shrinkage," *Biometrika*, vol. 81, no. 3, pp. 425–455, 1994.

[30] S. Zaslawski, Z. Yang, and L. Thévenaz, "On the 2D post-processing of Brillouin optical time-domain analysis," *J. Lightw. Technol.*, vol. 38, no. 14, pp. 3723–3736, Jul. 2020.

Ming Pan received the B.S. degree from the School of Physical Science and Technology, Tiangong University, Tianjin, China, in 2020. He is currently working toward the M.S. degree with the School of Precision Instruments and Opto-electronics Engineering, Tianjin University, Tianjin, China. His research focuses on optical fiber sensing.

Peidong Hua received the B.S. degree in 2019 from the School of Precision Instruments and Opto-electronics Engineering, Tianjin University, Tianjin, China, where he is working toward the Ph.D. degree. His research focuses on optical fiber sensing.

Zhenyang Ding received the B.S. degree in opto-electronics information engineering and the M.S. and Ph.D. degrees in optical engineering from Tianjin University, Tianjin, China, in 2008, 2010, and 2013, respectively. From 2013 to 2015, he was a Postdoctoral Researcher with the University of Maryland, College Park, MD, USA. He is currently an Associate Professor with the School of Precision Instruments and Opto-electronics Engineering, Tianjin University. His research interests include optical fiber sensing and optical coherence tomography.

Dongfang Zhu is currently a Researcher with Shanghai Aerospace Control Technology Institute, Shanghai, China.

Kun Liu received the B.S. degree in optoelectronics information engineering, and the M.S. and Ph.D. degrees in optical engineering from Tianjin University, Tianjin, China, in 2004, 2006, and 2009, respectively. He is currently a Professor with Tianjin University. His research interests include development of physics and chemistry sensing system based on optical fiber laser.

Junfeng Jiang received the B.S. degree from the Southwest Institute of Technology, Mianyang, China, in 1998, and the M.S. and Ph.D. degrees from Tianjin University, Tianjin, China, in 2001 and 2004, respectively. He is currently a Professor with Tianjin University. His research interests include fiber sensors and optical communication performance measurement.

Chenhuan Wang received the B.S. degree in 2017 from the School of Precision Instruments and Opto-electronics Engineering, Tianjin University, Tianjin, China, where he is currently working toward the Ph.D. degree. His research focuses on optical fiber sensing.

Haohan Guo received the B.S. degree from the School of Information Science and Engineering, Yanshan University, Qinhuangdao, China, in 2020. She is currently working toward the M.S. degree with the School of Precision Instruments and Opto-electronics Engineering, Tianjin University, Tianjin, China. Her research focuses on optical fiber sensing.

Teng Zhang received the B.S. degree in 2021 from the School of Precision Instruments and Opto-electronics Engineering, Tianjin University, Tianjin, China, where he is currently working toward the M.S. degree. His research focuses on optical fiber sensing.

Sheng Li received the B.S. degree in optoelectronics information science and engineering from the Changchun University of Science and Technology, Changchun, China, in 2021. He is currently working toward the M.S. degree with the School of Precision Instruments and Opto-electronics Engineering, Tianjin University, Tianjin, China. His research focuses on optical fiber sensing.

Tiegen Liu received the B.S., M.S., and Ph.D. degrees from Tianjin University, Tianjin, China, in 1982, 1987, and 1999, respectively. He is currently a Full Professor with the School of Precision Instrument and Optoelectronics Engineering, Tianjin University. His research interests include optical fiber sensing and photoelectric detection.